Nano Research

Open Access

Research Article

LM/PAN films with high thermal conductivity and excellent shielding performance for wearable electronics and devices

Quan Zhang[1,2], Junyou Luan[2], Zhong Zhao[2] ✉, Sirui Tan[2], Xiaoning Tang[2], Guangming Cai[1], Deshan Cheng[1,2] ✉, and Xin Wang[3] ✉

[1] State Key Laboratory of New Textile Materials and Advanced Processing Technologies, Wuhan Textile University, Wuhan 430200, China
[2] School of Textile Science and Engineering, Wuhan Textile University, Wuhan 430200, China
[3] School of Fashion and Textiles, RMIT University, Brunswick 3056, Australia

Cite this article: *Nano Research*, **2026**, *19*, 94908430. https://doi.org/10.26599/NR.2026.94908430

ABSTRACT: Materials with combined electromagnetic shielding and efficient thermal management functions are in high demand due to the rapid growth of electronic devices with excessive heat accumulation and electromagnetic interference. This work proposes a unique preparation strategy combining solution blow spinning, spraying and hot pressing to develop multi-layered liquid metal (LM)/polyacrylonitrile (PAN) films with well-disperse LM nanodroplets on PAN) fiber films. The in-plane thermal conductivity of the films reached 7.768 and 3.623 $W \cdot m^{-1} \cdot K^{-1}$ along the thickness direction, indicating 80 and 58 times higher than that of pure PAN film, respectively. The high thermal conductivity quickly dissipated the generated heat by electronic devices, helping address the issue of heat accumulation. In the X-band (8.2–12.4 GHz), the shielding effectiveness (SET) of the films was as high as 79.52 dB to effectively block electromagnetic wave interference. Based on the excellent performance of the films, a single-electrode triboelectric nanogenerator (HPP LM/PAN-TENG) pressure sensor was further developed. This sensor exhibited high sensitivity to pressure changes and accurately monitored both large and subtle human motions. More importantly, the sensor accurately captured the subtle features of early gait abnormalities with Parkinson's disease, providing evidences for early diagnosis. The LM/PAN films are easy to prepare and can be produced at a large scale, with a broad application potential in fields of thermal management of electronic devices, electromagnetic protection, and wearable sensing.

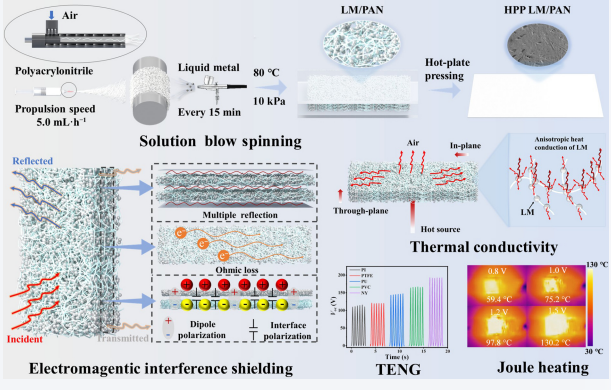

KEYWORDS: liquid metal, solution blow spinning, electromagnetic shielding, thermal management, triboelectric nanogenerator

1 Introduction

Liquid metal (LM), a pure metal or an alloy existing in liquid state at room temperature with high thermal conductivity and excellent electrical conductivity, has attracted significant attention in the field of compact electronic devices in recent years [1–3]. Specifically, the development of lightweight films featuring both high thermal conductivity and high electromagnetic interference (EMI) shielding performance is critical for addressing issues including heat accumulation and EMI [4–13]. Incorporating LM into composite materials has been reported as an effective way to tune critical properties such as electrical and thermal conductivity of the substrates [14–19]. However, the inherent characteristics of LM, including its propensity for oxidation, high surface tension and high fluidity, pose significant challenges for its leak-free encapsulation and uniform dispersion [20].

Solution blow spinning (SBS) is an emerging fiber fabrication technique and a versatile alternative to the widely used electrospinning process [21–26]. SBS utilizes a high-speed, pressurized gas stream to both propel the polymer solution and facilitate solvent evaporation [27–30]. Although electrospinning is extensively applied in both academic and industrial settings, its dependence on a high-voltage electric field introduces limitations in

Received: November 6, 2025; **Revised:** December 12, 2025
Accepted: January 12, 2026

✉Address correspondence to Zhong Zhao, zzhao@wtu.edu.cn; Deshan Cheng, chengcds@163.com; Xin Wang, xin.wang@rmit.edu.au

terms of safety, process stability, and scalability [31–34]. Conversely, SBS offers distinct advantages of relatively simpler settings, fewer variables, and imposes no requirements on the electrical conductivity of the solution or collector [35, 36]. This enables efficient production of polymeric fibrous materials which can be directly deposited onto target substrates [37]. These characteristics not only overcome certain bottlenecks associated with electrospinning but also open broader avenues for exploring new applications of fibrous materials. Furthermore, compared to melt-blowing, SBS employs polymer solutions. Therefore, the accompanying solvent evaporation and volumetric contraction during gas-stream drawing are more conducive to the formation of finer-diameter fibers. Like melt-blowing, SBS is also a continuous process, thus holding significant potential for large-scale production [38–40].

The distribution of LM has been an issue as its high surface tension and fluidity causing it to coalesce into large droplets during dispersion [41–43]. Besides, LM tends to leak when used as a filler, thus encapsulation within a polymer matrix is usually required [44–47]. Moreover, its surface is prone to oxidation upon dispersion, hindering its electrical conductivity in polymer composites [48–50]. To address these challenges, Li et al. dispersed LM in anhydrous ethanol under high-frequency agitation followed by spraying the dispersion onto a thermoplastic polyurethane (TPU) fibrous film for encapsulation [15]. Jiang et al. mixed sodium alginate (SA) with LM during dispersion to achieve a pre-coating effect with SA [16]. Yang et al. dispersed LM with dialdehyde xylan (DAX) in an ice-water bath under high-frequency conditions. By encapsulating the LM in polydimethylsiloxane (PDMS), a flexible triboelectric nanogenerator was subsequently prepared [51]. Previous research demonstrated that high-frequency dispersion and pre-coating methods could effectively address LM dispersion issues, while polymer encapsulation and mechanical sintering successfully mitigated the issues of leakage and surface oxidation.

This study reports an innovative method for fabricating a multilayered LM/PAN composite film by combining solution blow spinning with intermittent spraying of an LM/alcohol dispersion and hot-pressing treatment. The PAN film prepared via the SBS technique features a porous, three-dimensional (3D) interwoven structure that mechanically traps and anchors LM nanoparticles. Subsequent hot‑pressing enhances their encapsulation, removes surface oxides, and promotes an efficient thermal conduction network. The in-plane and through-plane thermal conductivity of the as-fabricated composite film reached 7.768 and 3.623 $W \cdot m^{-1} \cdot K^{-1}$, respectively, while a total electromagnetic shielding effectiveness (SET) of 79.52 dB within the X-band range was achieved. These results indicate outstanding thermal management and EMI shielding performance of the composite film. Furthermore, the composite film exhibited excellent Joule heating performance evidenced by a surface temperature of 130.2 °C under an applied voltage of 1.5 V. By further encapsulating the composite film with Ecoflex™, a single-electrode triboelectric nanogenerator-based pressure sensor was developed to effectively detect human motion with a potential for early pathological diagnosis in Parkinson's disease patients.

2 Experimental

2.1 Materials

Eutectic gallium-indium (EGaIn) liquid metal (composed of 85% Ga and 15% In, w/w, and with a melting point of 16 °C) was purchased from Dongguan Dingguan Metal Technology Co., Ltd. (Dongguan, China). Polyacrylonitrile (PAN, with a M_W of 85,000 and purity of 99%) was bought from Aladdin Scientific Corporation (Shanghai, China). Ecoflex™ was obtained from the Smooth-On, Inc. (Macungie, USA). N,N-Dimethylformamide (DMF) and ethanol were purchased from Sinopharm Chemical Reagent Co., Ltd. (Shanghai, China). All the chemicals used in this study were in analytical grade and used as received without further purification.

2.2 Preparation of LM/PAN films

PAN spinning solution was first prepared by adding 3 g PAN powder to 15.75 g DMF followed by continuous stirring at 70 °C in an oil bath for 5 h until a homogeneous solution was obtained. A beaker of solid LM was kept in a 60 °C water bath for 5 min to promote a complete phase transition to the liquid state. 1.5 mL (approximately 10 g) molten LM was loaded into a 5 mL syringe and subsequently 30 mL anhydrous ethanol added into the same syringe. A uniform LM suspension was then achieved after 10 mins' ultrasonicating the LM/ethanol mixture with a JY92-II ultrasonic cell disruptor (Xinyi Ultrasonic Equipment Co., Ltd., Ningbo, China). The as prepared LM suspension was stored at room temperature for subsequent use.

LM/PAN films were fabricated via solution blow spinning, as illustrated in Fig. 1(a). The as-prepared PAN solution was filled into a 10 mL syringe with a coaxial needle consisting a 15-G outlet for the polymer solution and a 20-G outlet for the air flow. The air inlet of the coaxial needle was linked to an air pump to supply a gas flow at a pressure of 14.71 kPa (0.15 $kg \cdot cm^{-2}$). During spinning process, the air flow constantly blew the polymer solution extruded from the syringe (5.0 $mL \cdot h^{-1}$). A rotating drum with a distance of 30 cm from the needle tip was used to collect the blown fibers into a PAN film. The entire spinning process was conducted under controlled environmental conditions, i.e., 25 ± 2 °C and relative humidity of 40% ± 2%.

To incorporate the LM into the fiber matrix, the LM suspension was intermittently (15-min intervals) sprayed onto the surface of the films using an airbrush at 30 cm from the colleting drum. The gas flow for the spraying process was supplied by an air pump at 196.133 kPa (2 $kg \cdot cm^{-2}$). The as-prepared LM/PAN films were then stored at room temperature to allow for the complete evaporation of residual solvent. A consolidation step was performed by hot-pressing the composite film at 10 MPa, 80 °C and for 5 s using a hot plate pressing machine. The as-prepared hot-plate-pressed LM/PAN film was coded as HPP LM/PAN.

2.3 Characterization of LM/PAN films

The surface morphology of pure PAN, LM/PAN, and HPP LM/PAN was characterized by scanning electron microscopy coupled with energy-dispersive X-ray spectroscopy (SEM-EDS, ZEISS Gemini 300, Germany). The crystal structure of the pure PAN fiber film and the HPP LM/PAN composite film were examined using an X-ray diffractometer (XRD, Rigaku Smart Lab SE, Japan) with Cu Kα radiation over a 2θ range from 10° to 80°. The surface chemical states of the as-prepared composite films were analyzed by X-ray photoelectron spectroscopy (XPS, Thermo Scientific ESCALAB 250Xi, USA).

2.4 Thermal conductive performance

The specific heat capacity (C_p) and thermal diffusivity (α) of the

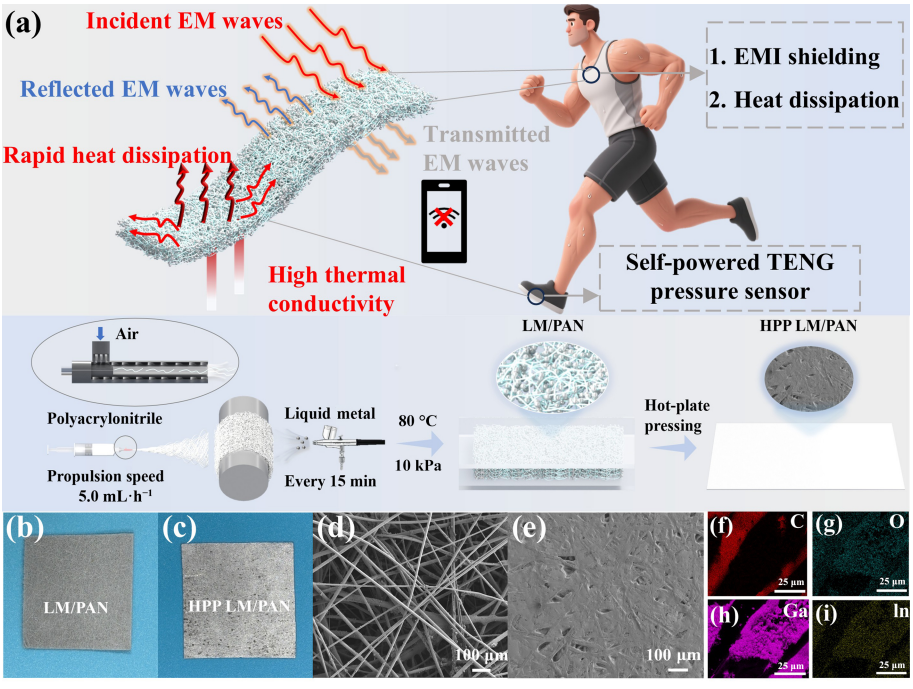

Figure 1 (a) Schematic diagram of the fabrication process of LM/PAN composite film. (b)–(e) Optical and SEM images of LM/PAN and HPP LM/PAN. (f)–(i) EDS images of HPP LM/PAN.

PAN, LM/PAN, and HPP LM/PAN films were measured at 25 °C using a laser flash analyzer (NETZSCH LFA 467, Germany). The measurements were performed in both the in-plane and through-plane directions to measure the anisotropic thermal transport. The bulk density (ρ) of each film was determined by the water displacement method. Based on these parameters, the anisotropic thermal conductivity λ ($\lambda_{\text{in-plane}}$ and $\lambda_{\text{through-plane}}$) was calculated using Eq. (1) [4].

$$\lambda = C_p \times \alpha \times \rho \tag{1}$$

The thermal conductivity of the films was also tested on a hotplate. The composite film was placed on the surface of the heating plate with a stabilized temperature of 65 °C. Meanwhile, the temperature of the surface of the film was monitored by an infrared camera (HIKMICRO TPK20-3A, China).

2.5 EMI shielding performance

The EMI shielding performance within the X-band frequency was measured in the range (8.2–12.4 GHz) for pure PAN, along with HPP LM/PAN composite films with two different thicknesses (i.e., LM spraying intervals of 15 and 30 min, denoted as HPP LM/PAN-15 and HPP LM/PAN-30, respectively). The measurements were carried out using a vector network analyzer (Agilent E5071C, USA). Each sample was cut into a 3 cm × 3 cm square to fit the waveguide setup. A thru-reflect-line (TRL) calibration was performed to minimize measurement errors prior to the scanning. The scattering parameters (S_{11}, S_{12}, S_{22}, and S_{21}) were recorded and subjected to the calculation of relevant EMI shielding performance indexes using Eqs. (2)–(7) [52, 53]

$$R = |S_{11}|^2 = |S_{22}|^2 \tag{2}$$

$$T = |S_{21}|^2 = |S_{12}|^2 \tag{3}$$

$$A = 1 - R - T \tag{4}$$

$$SE_R = -10\lg(1-R) \tag{5}$$

$$SE_A = -10\lg(T/(1-R)) \tag{6}$$

$$SE_T = SE_R + SE_A + SE_M \tag{7}$$

where T, R, and A represent transmittance, reflectance, and absorptance, respectively. The parameters SE_R, SE_A, SE_M, and SE_T correspond to the shielding effectiveness reflected from the perspectives of reflection, absorption, multiple internal reflections, and total shielding effectiveness, respectively.

It should be noted that the SE_M contribution is typically considered negligible and can be omitted when the SE_T exceeds 15 dB [54].

2.6 Joule heating performance

To test the Joule heating performance, the LM/PAN composite film was connected to a direct current (DC) power supply (MAISHENG MS-303D, China) at gradient voltages of 0.4, 0.8, 1, 1.2, and 1.5 V. The corresponding temperature evolution on the film surface was monitored in real-time using an Infrared thermal imager. To further assess the stability of the electrothermal behavior, a constant voltage of 1 V was applied to the film for 1 h for the surface temperature monitoring.

2.7 Triboelectric nanogenerator (TENG)

A single-electrode mode TENG featuring a sandwiched structure was fabricated based on the LM/PAN composite film and denoted as HPP LM/PAN-TENG. More specifically, the LM/PAN composite film served as the middle electrode layer while two Ecoflex™ elastomer layers functioned as the top and bottom

triboelectric layers. To fabricate the HPP LM/PAN-TENG, two precursors of the liquid silicone rubber (Ecoflex™) were thoroughly mixed in a 1:1 ratio (w/w) to form a total of 20 mL liquid-state Ecoflex™. 10 mL of the liquid-state Ecoflex™ was subsequently poured into a custom mold. Then, the LM/PAN composite film was positioned onto the uncured Ecoflex™ in the mold, and a copper foil attached with a lead wire was placed on the surface of the LM/PAN composite film. Finally, the rest 10 mL liquid-state Ecoflex™ was used to encapsulate the entire assembly. The as-prepared flexible electrode was then cured in an oven at 60 °C for 20 min followed by subsequent demolding after solidification.

3 Results and discussion

3.1 Characterization

The optical and SEM-EDS images of LM/PAN and HPP LM/PAN films as shown in Fig. 1. Numerous LM nanoparticles are deposited on the fiber surfaces after spraying with the LM dispersion (Figs. 1(b)–1(d), and Figs. S1 and S2 in the Electronic Supplementary Material (ESM)). Following the hot-pressing process, the fibers and LM merge into a dense film (Fig. 1(c)) with LM nanoparticles clearly visible on the surface (Fig. 1(e)). Moreover, as evidenced by the SEM image captured from its cross-section (Fig. S3 in the ESM), the inter-fiber spaces inside the original LM/PAN film were squeezed out during the hot-pressing process, leading to the formation of densely compacted bulk of the HPP LM/PAN. The color changed from gray to a metallic silvery-white during the fabrication process. Distinct signals of C, O, Ga, and In elements appeared in the EDS mapping of the composite film (Figs. 1(f)–1(i)). These elemental distribution and composition results confirmed the successful integration of PAN and LM.

Two distinct characteristic peaks appeared at 16.7° and 28.8° in the XRD pattern of pure PAN (Fig. 2(a)), corresponding to the (100) and (200) crystallographic planes, respectively. After the introduction of LM, the intensity of the characteristic PAN peaks significantly decreased while two new diffraction peaks emerged at 30.3° and 35.7°. The new peaks are assigned to the (222) and (400) planes of LM, respectively, according to the reported data [5].

The surface chemical state of the HPP LM/PAN composite was further confirmed by X-ray photoelectron spectroscopy (XPS). The wide-scan XPS spectrum of HPP LM/PAN (Fig. 2(b)) confirms the presence of carbon (C), oxygen (O), gallium (Ga), and indium (In). The high-resolution C 1s spectrum (Fig. 2(c)) can be fitted into three peaks at 284.8, 286.4, and 288.0 eV, corresponding to C–C, C–O, and C=O bonds, respectively. In the O 1s spectrum (Fig. 2(d)), the dominant peak observed at 530.9 eV is associated with metal–oxygen bonds. Intense peaks of Ga^{3+} appear at 1144.6 and 1117.9 eV in the Ga 2p spectrum (Fig. 2(e)), and minor contributions at 1142.65 and 1115.5 eV can be assigned to Ga^0. Similarly, the In 3d spectrum (Fig. 2(f)) is composed of two peaks at 445.3 and 438.6 eV, corresponding to In_2O_3 and metallic In (In^0), respectively [5, 17].

3.2 Thermal conductive performance

Thermal conductivity is a critical parameter for evaluating the potential application of materials in thermal management of compact electronic devices. The thermal diffusivity (α) of the films was measured to determine their thermal conductivity (λ). A thermal conductivity testing device was self-built using a heating plate and an Infrared thermal imager (Fig. 3(a)). The three samples were attached to the hot plate with a temperature maintained at 65 °C. As shown in Fig. 3(b), the surface temperature of the HPP LM/PAN composite film reached 48.8 °C after 5 min, lower than that of PAN (55.7 °C) and LM/PAN (52.9 °C). Temperature-time

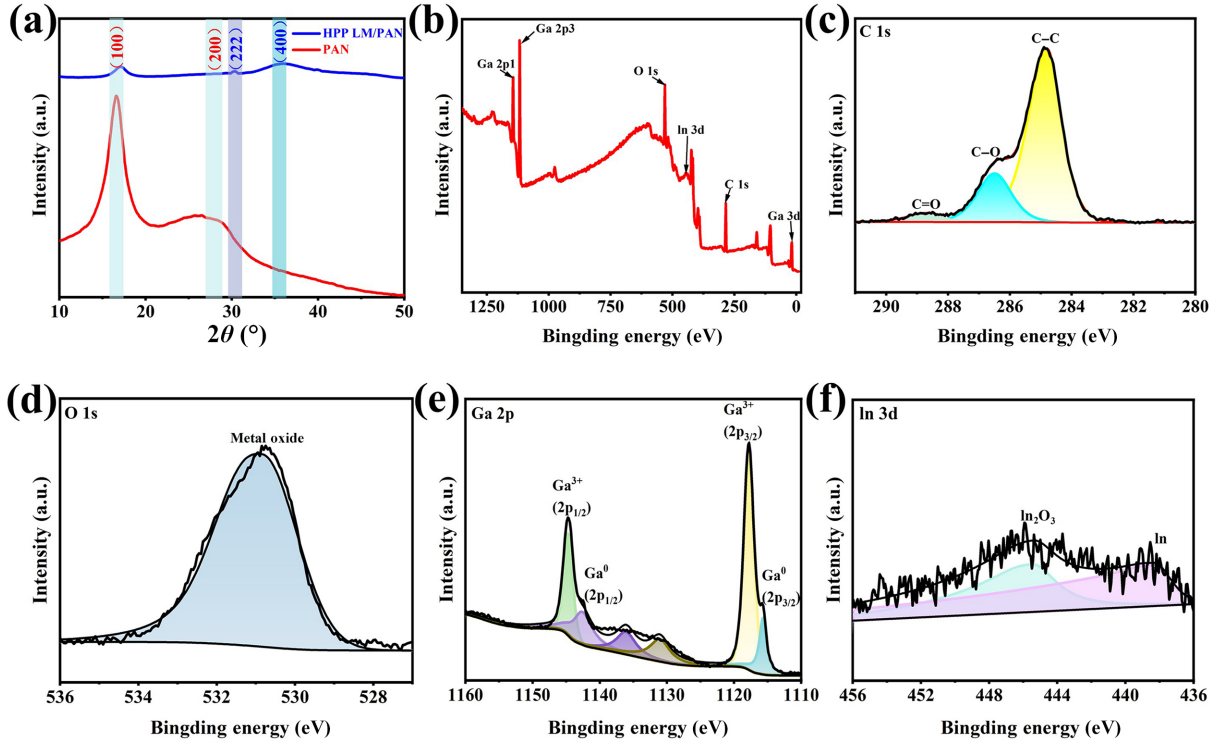

Figure 2 (a) XRD spectra of pure PAN and HPP LM/PAN. (b) XPS wide scan spectrum of HPP LM/PAN. (c)–(f) The high- resolution XPS spectra of C 1s, O 1s, Ca 2p, and In 3d.

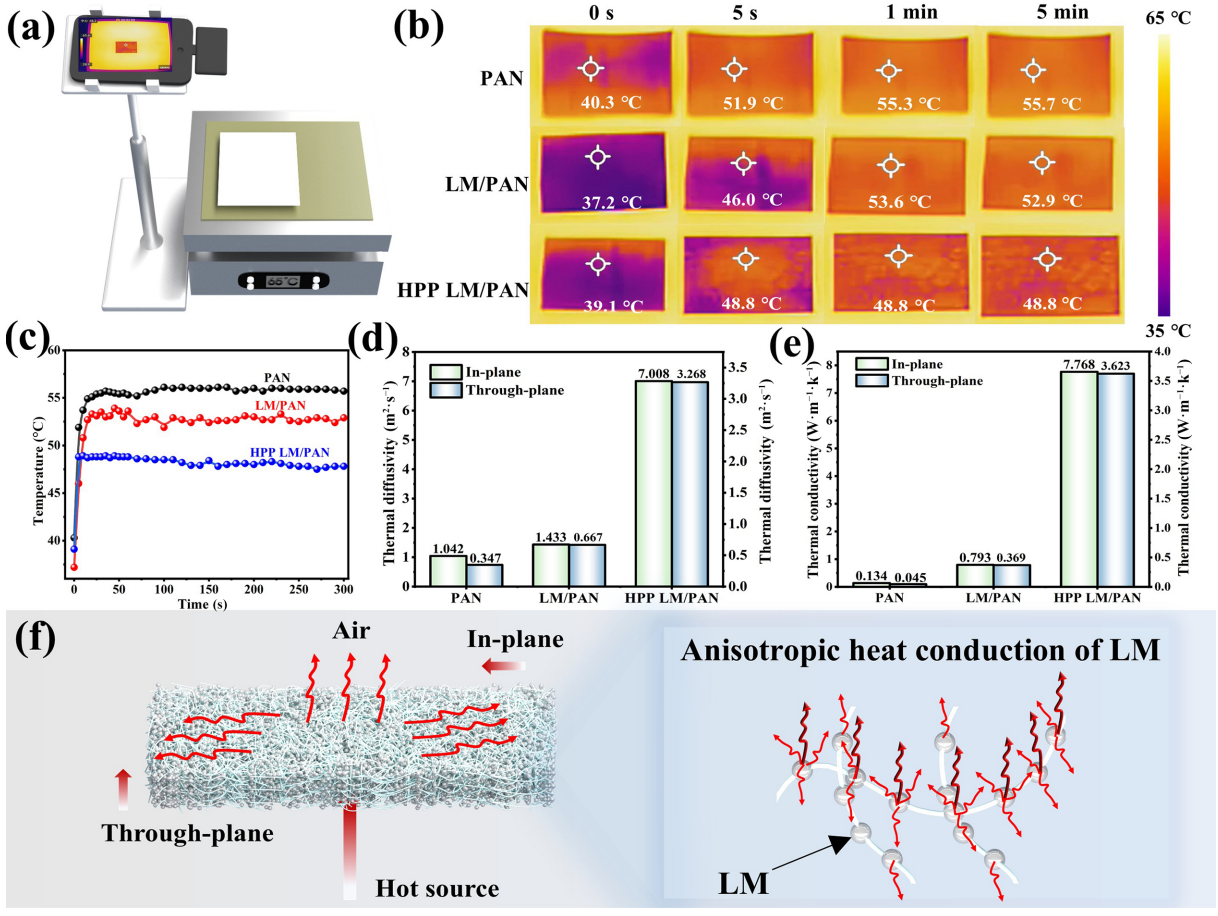

Figure 3 (a) Self-built equipment for thermal conductive performance measurements. (b) Infrared thermal images captured at different time, (c) temperature–time curves, (d) in-plane and through-plane bar charts of thermal diffusion, and (e) thermal conductivity of PAN, LM/PAN, and HPP LM/PAN. (f) Proposed thermal conduction mechanism of LM/PAN.

curves presented in Fig. 3(c) indicates that the LM/PAN composite film rapidly diffused heat into the ambient environment and maintained a much lower surface temperature, demonstrating its significant potential for application in thermal management of small-scale electronic devices.

Figure 3(d) presents the thermal diffusivity of the PAN, LM/PAN, and HPP LM/PAN films, in both the in-plane and through-plane directions. Data analysis reveals that the in-plane thermal diffusivity of the PAN and LM/PAN films is 1.042 and 1.433 $mm^2 \cdot s^{-1}$, respectively. However, the in-plane thermal diffusivity of the HPP LM/PAN film is 7.008 $mm^2 \cdot s^{-1}$, approximately 5.7 times higher than that of the pristine PAN film. In contrast, the through-plane thermal diffusivity of the three samples is lower, e.g., 0.347, 0.667, and 3.268 $mm^2 \cdot s^{-1}$ for PAN, LM/PAN, and HPP LM/PAN, respectively. It is worth noting that the through-plane thermal diffusivity of the HPP LM/PAN composite film is about 8 times greater than that of the PAN film. The thermal conductivity (λ) of the three samples was calculated from their thermal diffusivity, specific heat capacity, and density. As shown in Fig. 3(e), the in-plane thermal conductivity ($\lambda_{in\text{-}plane}$) values for PAN and LM/PAN are 0.134 and 0.793 $W \cdot m^{-1} \cdot K^{-1}$, respectively. The incorporation of LM nanoparticles enhanced the thermal conductivity of PAN by a factor of 5.9 due to the improved heat transfer pathways formed along the fiber surfaces. After hot-pressing, the intimate integration of LM with PAN disrupted the surface oxide layer on the LM nanoparticles, enabling the covering of LM onto the PAN fibers effectively. This structural optimization resulted in a remarkable in-plane thermal conductivity of 7.768 $W \cdot m^{-1} \cdot K^{-1}$ for the HPP LM/PAN film. Notably, it is 56.9 times higher than the conductivity of the pristine PAN film. The through-plane thermal conductivity ($\lambda_{through\text{-}plane}$) values are 0.045, 0.369, and 3.623 $W \cdot m^{-1} \cdot K^{-1}$ for PAN, LM/PAN, and HPP LM/PAN, respectively. Although the through-plane thermal conductivity remains substantially lower than that of in-plane direction, the value for the HPP LM/PAN film is roughly 80 times greater than that of PAN.

A schematic illustration of the proposed thermal conduction mechanism of the LM/PAN composite film is shown in Fig. 3(f). Heat generated form a source is transferred through the LM/PAN film, where the embedded LM facilitates multidirectional heat propagation, ultimately promoting rapid heat dissipation into the surrounding atmosphere.

3.3 EMI shielding

The as-prepared LM/PAN composite films demonstrated promising EMI shielding performance. As depicted in Fig. 4(a), the electrical resistance of the film decreased from 7.46 to 0.50 Ω with the increase in the film thickness, indicating the formation of an efficient conductive network by the LM on the surface. As reflected by the average reflectance (R) and absorptance (A) coefficients of the three samples (Fig. 4(b)), the pure PAN film features a lower R than A. In contrast, after the incorporation of LM, the composite

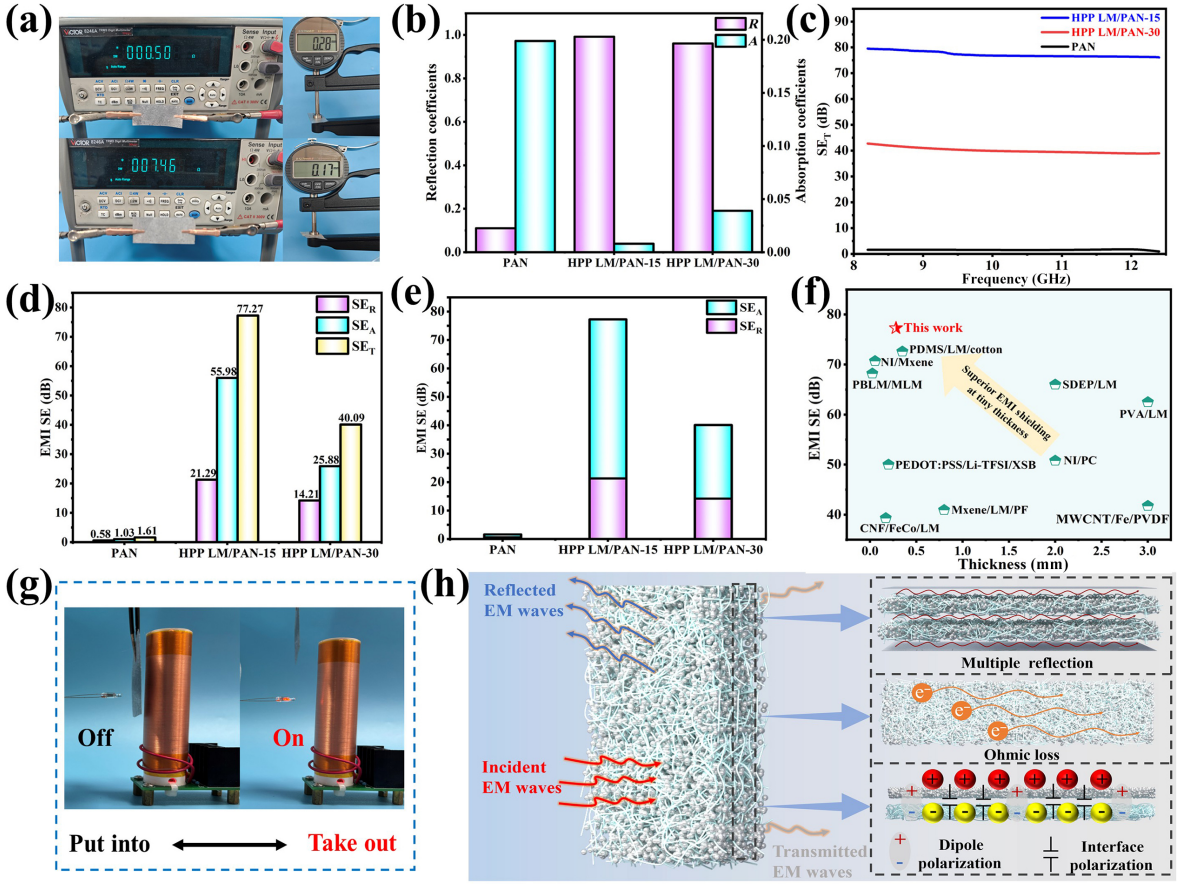

Figure 4 (a) Surface resistance of HPP LM/PAN-15 and HPP LM/PAN-30. (b) Column plots of average reflection and absorption coefficients, (c) SE_T data plots and ((d) and (e)) average SE_R, SE_A, and SE_T of PAN, HPP LM/PAN-15, and HPP LM/PAN-30 in X-band. (f) Comparative analysis to different EMI shielding materials as reported in the past five years. (g) Proof of concept device to demonstrate the EMI performance of HPP LM/PAN and (h) its proposed electromagnetic shielding mechanism diagram.

film shows an R value substantially greater than A. This difference can be attributed to the fact that R is closely related to surface impedance while A is more dependent on thickness. These results confirm that the fabricated LM/PAN composite films have a lightweight and thin profile but possess a high electrical conductivity.

As shown the total EMI shielding effectiveness (SE_T) results in Fig. 4(c), the LM/PAN composite films exhibit outstanding EMI shielding performance governed by both film thickness and electrical conductivity. HPP LM/PAN-15 demonstrates the highest shielding capability evidenced by a maximum SE_T value of 79.52 dB, followed by HPP LM/PAN-30 with a SE_T value of approximately 42.75 dB. Owing to the electrical insulation properties of PAN fibers, the pristine PAN film allowed for substantial transmission of electromagnetic waves, resulting in a low SE_T value. Furthermore, the frequency-dependent SE_T values across the X-band are also presented in Fig. 4(c), demonstrating a slight decreasing trend with the the increase of frequency. This result suggests that the EMI shielding capability of the LM/PAN films is marginally higher for lower frequencies (longer wavelengths) than higher frequencies (shorter wavelengths).

The average SE_R, SE_A, and SE_T values of the three samples within the X-band are plotted in Fig. 4(d). The average SE_T value for PAN is only 1.16 dB, whereas the values for LM/PAN-15 and LM/PAN-30 are 77.27 and 40.09 dB, respectively. As shown in Fig. 4(e), the average SE_A values for all three composite samples are greater than their corresponding SE_R values. This result indicates that the attenuation of electromagnetic waves within the materials (via absorption) surpasses the attenuation caused by surface reflection, and it plays a dominant role in EMI shielding. To taking the film thickness into consideration, the specific shielding effectiveness (SE/d) was also calculated. As shown in Figs. S4 and S5 in the ESM, the LM/PAN composite film achieves an average SE/d of 276.17 dB·mm^{-1} at a thickness of 0.28 mm and 235.71 dB·mm^{-1} at 0.17 mm. Comparison of SE_T performance between the as prepared LM/PAN films and other metal-based EMI shielding materials reported in literature was conducted from the perspective of thickness, as shown in Fig. 4(f). The comparison highlights that the LM/PAN film not only possesses a thin and lightweight profile but also delivers excellent EMI shielding performance within the X-band.

A proof-of-concept device was constructed using a Tesla coil and a green light-emitting diode (LED), where the LED lights up when placed near the energized coil. As shown in Fig. 4(g), when the PAN fiber film was placed between the Tesla coil and the LED, the LED remained illuminated. However, when the LM/PAN film was placed in between them, the LED was extinguished immediately. The LED instantly relighted upon the removal of the LM/PAN shield, visually confirming the effective EMI shielding capability of the composite film.

Figure 4(h) schematically illustrates the proposed EMI shielding mechanism. When incident electromagnetic waves impinge on the

surface of the LM/PAN film, a portion of which are immediately reflected into the air due to the abundant free electrons within the highly conductive components. The remaining waves penetrate the film and undergo repeated internal reflections between the multi-layered LM/PAN interfaces. This multi-reflection process significantly prolongs the propagation path, thereby enhancing energy dissipation within the lossy medium. Furthermore, direct interaction between the electromagnetic waves and the LM results in energy dissipation in the form of ohmic loss. Both dipole polarization and interface polarization phenomena, induced by the LM-PAN heterostructure, contribute to additional attenuation across different frequencies. Consequently, the residual electromagnetic waves are unable to penetrate the LM/PAN film easily and are ultimately absorbed and converted into thermal energy. In summary, the synergistic effect of excellent electrical conductivity and well-designed interfacial architecture enables the outstanding EMI shielding performance at a minimal film thickness for the composite film.

3.4 Joule heating

The Joule heating performance of the LM/PAN composite film was evaluated in a low input voltage range to assess its reliability for practical applications. Figure 5(a) conforms that the film has a stable electrical resistance obeying the Ohm's law. As shown in Fig. 5(b), the steady-state temperature of the film could be readily tuned by adjusting the applied voltage from 0.4 to 1.5 V. Specifically, temperatures of 34.8, 59.4, 75.2, 97.8, and 130.2 °C were achieved at 0.4, 0.8, 1, 1.2, and 1.5 V, respectively. The corresponding Infrared thermal images demonstrate a uniform temperature distribution across the composite film (Fig. 5(c)). Moreover, due to the encapsulation of LM by the PAN matrix, the HPP LM/PAN exhibited prominent stability without LM leakage being observed after the shelf-heating process (Video S1 in the ESM) as well as repeated pressing cycles (Video S2 in the ESM). Owing to the superior electrical and thermal conductivity of LM, the LM/PAN film could reach thermal saturation within merely 10 s. Conversely, the film cooled down to room temperature within 20 s upon switching off the power (Fig. 5(d)).

Durability is a critical indicator for practical applications. The surface temperature of the LM/PAN composite film was measured under a constant voltage of 1 V for 1 h. As shown the Fig. 5(e), the film has the capability to withstand prolonged exposure to elevated temperatures. The ice-melting capability of the LM/PAN film was conducted by placing a vial filled with ice was on the film surface, as illustrated in Fig. 5(f). After applying a voltage of 1.2 V, the ice melted completely and transformed into liquid water within 6 min. Notably, no observable leakage of LM from the film surface was found at the bottom of the vial. In summary, the LM/PAN composite film demonstrated exceptional Joule heating performance, reaching a surface temperature of 130.2 °C with an applied voltage of only 1.5 V.

3.5 Triboelectric nanogenerators

The excellent electrical conductivity of LM makes it an ideal choice for the electrode in TENGs. Figure 6(a) illustrates the schematic structure and operational principle of the single-electrode mode HPP LM/PAN-TENG with a sandwich configuration of a 4 cm × 4 cm LM/PAN composite film connected to a wire via a copper foil

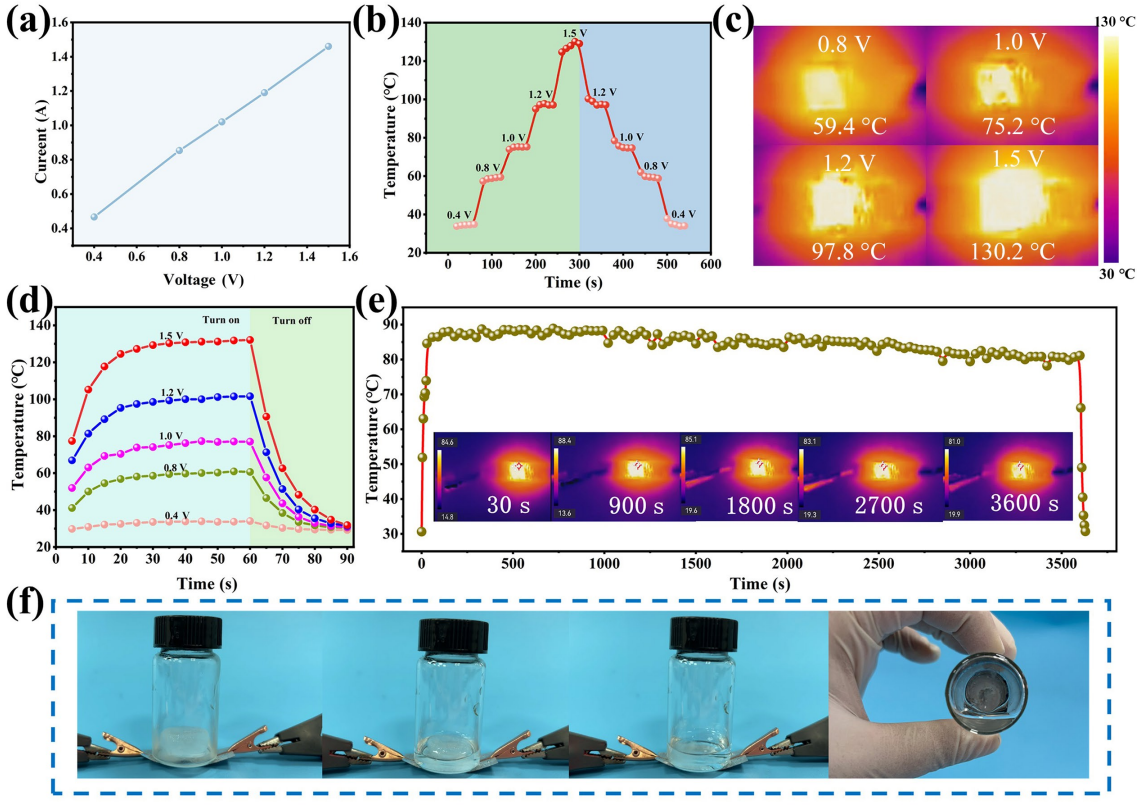

Figure 5 (a) *I–V* curve of HPP LM/PAN film. (b) Cyclic electro-thermal conversion at 0.4–1.5 V, (c) Infrared thermal images at different voltages, (d) temperature variation curves at different input voltages, and (e) temperature variation curve under a constant voltage of 1 V for 1 h of HPP LM/PAN. (f) Ice-melting test on the HPP LM/PAN film at an applied voltage of 1.2 V.

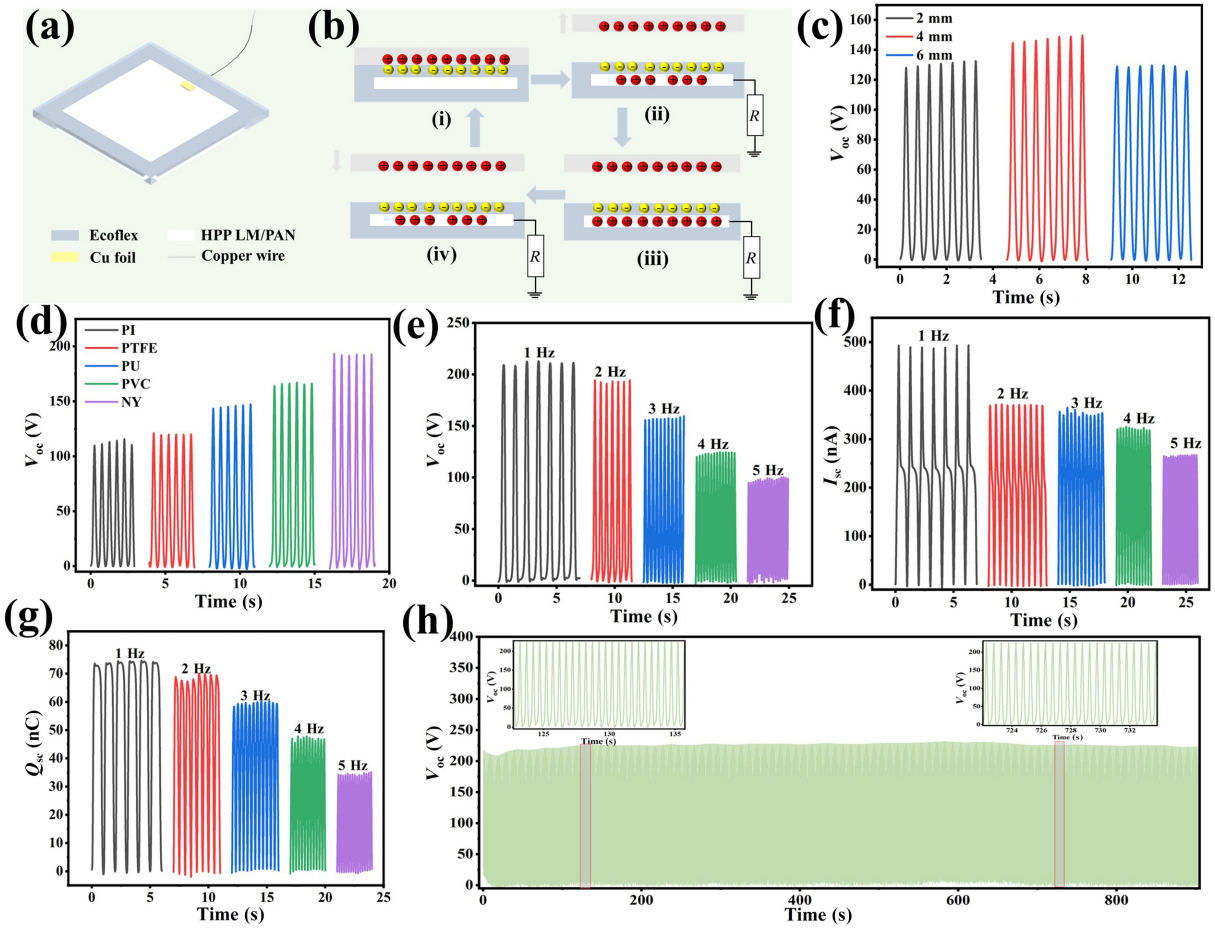

Figure 6 (a) Structure diagram and (b) schematic diagram of the working mechanism of HPP LM/PAN-TENG. (c) V_{oc} of Ecoflex packages with different thicknesses. (d) V_{oc} of HPP LM/PAN-TENG in contact and separation with different materials. (e)–(g) V_{oc}, I_{sc}, and Q_{sc} of HPP LM/PAN-TENG at different operating frequencies. (h) Performance stability during 1800 mechanical shock cycles.

and encapsulation of Ecoflex™ elastomer. The Ecoflex™ layer forms the encapsulation to prevent potential LM leakage, and it also serves as the negative triboelectric material with excellent flexibility and biocompatibility.

As demonstrated in Fig. 6(b), when the HPP LM/PAN-TENG is brought into contact with a positive triboelectric layer, positive charges are generated at the interface. An equal number of negative charges with opposite polarity is induced on the Ecoflex™ surface. At this stage, due to the complete electrostatic equilibrium between the triboelectric charges, no electron flow occurs in the external circuit. As the positive triboelectric layer separates from the Ecoflex™, the LM/PAN electrode generates a positive potential to compensate the negative charges on the Ecoflex™ surface. During this separation process, electrons flow from the electrode to the external circuit, generating a measurable transient current signal. When the positive triboelectric layer moves downward and approaches the Ecoflex™ again, electrons are driven back from the circuit to the LM/PAN electrode under electrostatic induction. This periodic contact-separation cycle produces an alternating current output ((i)–(iv)).

To investigate the influence of triboelectric layer thickness on the electrical output of the HPP LM/PAN-TENG, Ecoflex™ layers of different thicknesses (2, 4, and 6 mm) were used to encapsulate the LM/PAN composite film. A polyurethane (PU) film was uded as the positive triboelectric layer, with tests conducted under a constant frequency (2 Hz) and force (~ 20 N). The results are shown in Fig. 6(c). The data indicate that the 4-mm-thick Ecoflex™ layer yields the highest output voltage of 147.5 V, compared to 131 and 127 V for the 2-mm and 6-mm thicknesses, respectively. This behavior can be attributed to the fact that an over thin Ecoflex™ layer undergoes insufficient deformation, leading to a reduced effective contact area with the underlying conductive LM/PAN layer, thereby impairing voltage output. Conversely, an excessively thick Ecoflex™ layer directly limits the intimacy of contact between the Ecoflex™ and the LM/PAN electrode. Subsequently, the 4-mm-thick Ecoflex™ was selected to study the effect of different positive triboelectric materials, including polyimide (PI), polytetrafluoroethylene (PTFE), polyvinyl chloride (PVC), and nylon (NY), on the electrical output (Fig. 6(d)). Under identical testing conditions (2 Hz, ~ 20 N), the NY film generates the highest output voltage of approximately 193 V, whereas PI produces a relatively weaker output of about 112 V. This variation is due to the differences in triboelectric polarity and electron affinity among these materials. Therefore, NY was selected as the optimal positive triboelectric layer for the HPP LM/PAN-TENG.

The open-circuit voltage (V_{oc}), short-circuit current (I_{sc}), and transferred short-circuit charge (Q_{sc}) of the HPP LM/PAN-TENG were measured at different operating frequencies (Figs. 6(e)–6(g)) [55, 56]. Analysis of the data shows that V_{oc}, I_{sc}, and Q_{sc} progressively decrease as the frequency increasing from 1 to 5 Hz. This decline is

attributed to insufficient charge accumulation on the Ecoflex™ surface and its inflexibility to keep pace with the rapid contact-separation cycles at higher frequencies with a reduced effective contact area. Despite this frequency dependence, the fabricated HPP LM/PAN-TENG demonstrates excellent electrical output performance at lower frequencies, achieving values of 211 V for V_{oc}, 489 nA for I_{sc}, and 73 nC for Q_{sc}. The electricity generated by the flapping action on the HPP LM/PAN TENG can light up green LED arrays (Video S3 in the ESM). Finally, an anti-fatigue test was performed on the HPP LM/PAN-TENG at 2 Hz and an applied force of approximately 30 N (Fig. 6(h)). The device maintained a stable V_{oc} of 203 V even after 1800 consecutive cycles, confirming its robust operational durability.

3.6 Pressure sensors

The output voltage of the HPP LM/PAN-TENG is intrinsically dependent on the operational frequency and applied mechanical pressure. This correlation was leveraged to implement the device as an effective pressure sensor for motion detection. As shown in Fig. 7(a), the HPP LM/PAN-TENG was placed on a universal testing machine (DR-507ASQ, China) to investigate its resilience when subjected to compression under different forces. Figure 7(b) presents the force-displacement curves obtained at 20, 40, 60, and 80 N. The curves exhibit a convex region in their middle section, the extent of which increases with applied force. This characteristic profile arises from the sequential load-bearing process. For example, the initial stress was initially absorbed by the surface Ecoflex™ layer followed by the internal LM/PAN composite film before the deformation of the entire HPP LM/PAN-TENG structure. Despite this complex response, the HPP LM/PAN-TENG demonstrates excellent resilience. Furthermore, even after 1000 compression cycles at 40 N (Fig. 7(c)), its elastic recovery is nearly unaffected.

To evaluate the practical application of the HPP LM/PAN-TENG as a pressure sensor, its performance in human motion detection was explored. As depicted in Figs. 7(d)–7(f), when the device was pressed using two fingers, three fingers, and the full palm, the output signal varied distinctly with increasing contact area and applied pressure, reaching a maximum amplitude of approximately 273 V under palm compression. The HPP LM/PAN-TENG was also attached to the heel to monitor different gait patterns during walking, jogging, and fast running (Figs. 7(g)–7(i)). The resultant data displays distinct peak profiles and output voltages for each activity. During normal walking, the signals show broader peaks at a lower frequency. A characteristic double-peak profile with an increased frequency was obtained for jogging. In contrast, a sharp, high-frequency single peak patten with an output voltage reaching about 204 V was achieved via fast running. These results confirm that the HPP LM/PAN-TENG functions as a rapidly varying and fast-responsive pressure sensor, demonstrating its reliability for motion detection and activity monitoring applications.

The as-fabricated HPP LM/PAN-TENG pressure sensor exhibits high dynamic responsiveness and rapid signal recovery, demonstrating exceptional sensitivity to foot movements. This characteristic enables precise capture of gait patterns, offering a novel diagnostic tool for detecting pathologies (such as early-stage Parkinson's disease) based on biomechanical parameters of the foot. Three sensing areas were designated on the sole, i.e., the heel (Area 1), midfoot (Area 2) and forefoot (Area 3). Figures 8(a) and 8(b) present the voltage signals recorded from these three regions

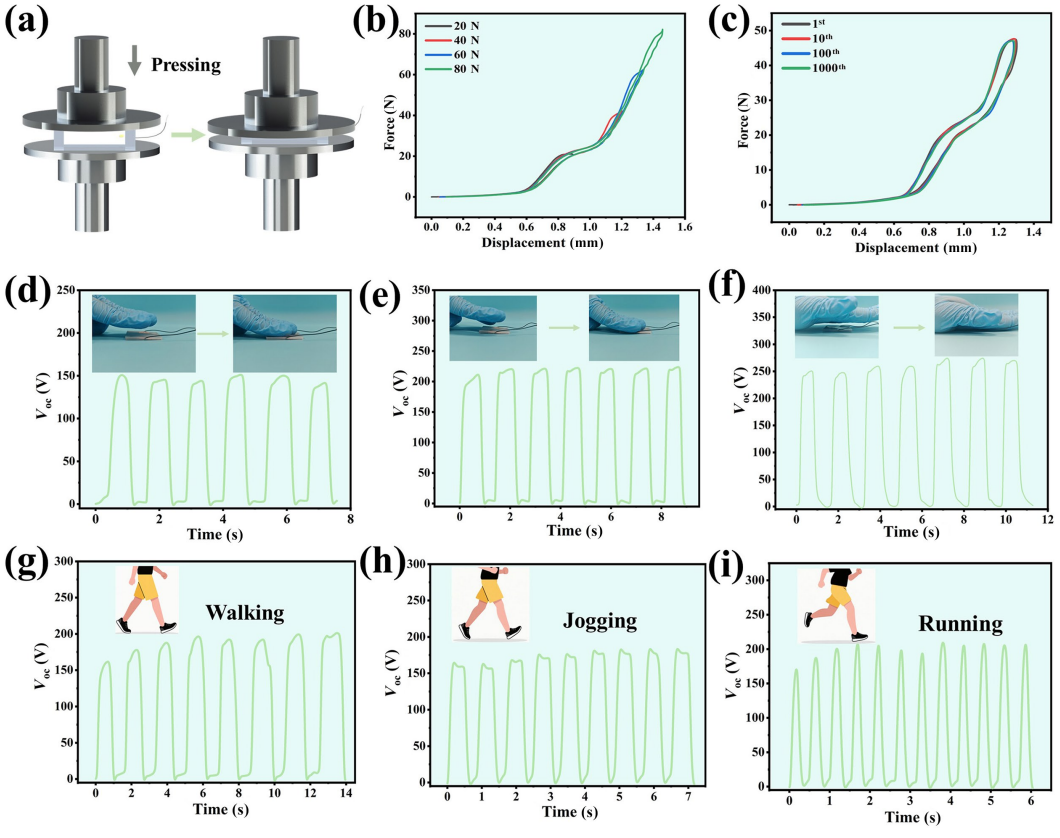

Figure 7 (a) Compression schematic diagram, (b) force and displacement curves under different pressures, and (c) cycle diagram of 1000 compressions under 40 N pressure of HPP LM/PAN-TENG. (d)–(f) Voltage output changes of HPP LM/PAN-TENG under finger and palm pressing and ((g)–(i)) different movements.

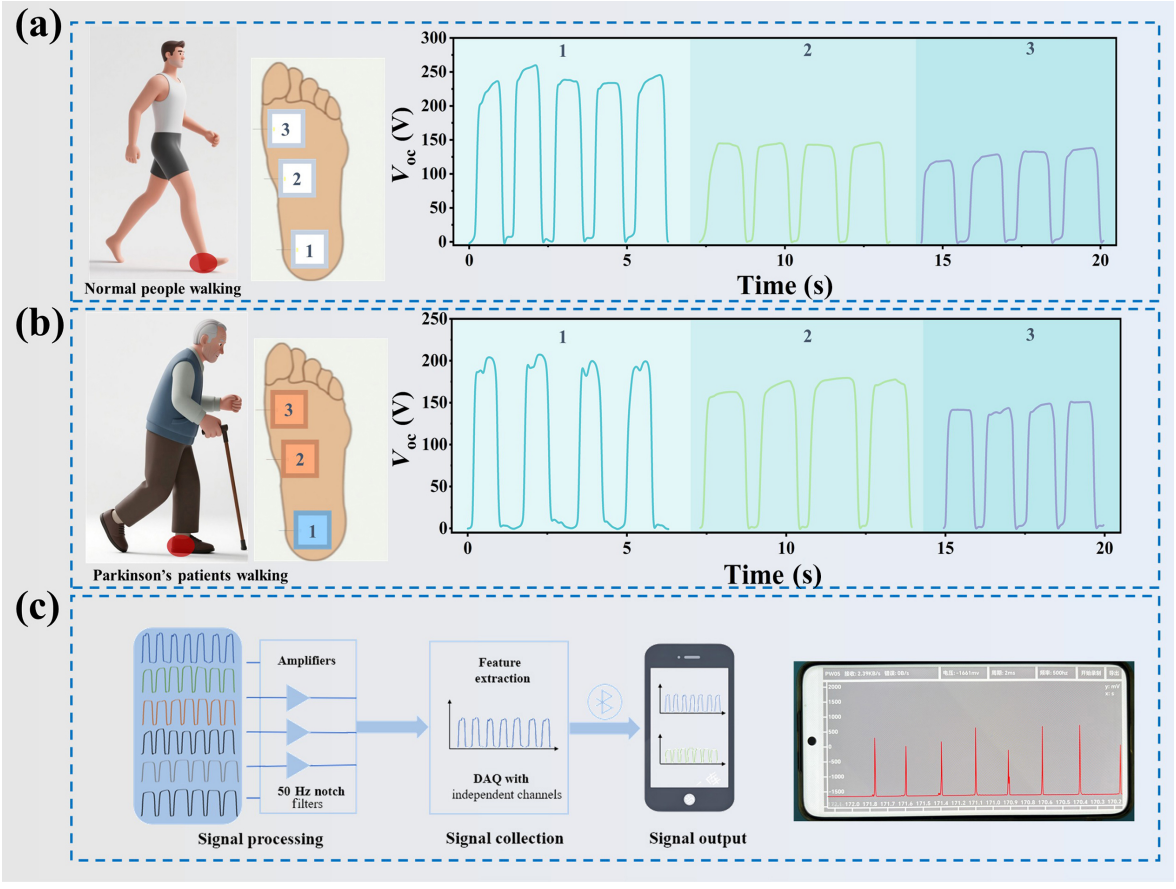

Figure 8 (a) Distribution map of three regions of foot pressure and their corresponding output voltages of normal walking and (b) Parkinson's patients walking. (c) Processing diagram for transmitting output signals to a mobile phone.

during normal walking and simulated Parkinsonian gait, respectively. Significant variations in signal patterns can be observed across the three areas. During normal walking, the heel serves as the primary force application point, resulting in a highest signal amplitude in Area 1. In contrast, the Parkinsonian gait, characterized by slower steps, heel trembling, and reduced applied pressure, leads to a noticeable decrease in both signal frequency and amplitude in Area 1, accompanied by a distinct double-peak profile. Conversely, the signal intensity in Areas 2 and 3 is markedly higher than healthy subjects. This shift is attributed to the redistribution of plantar pressure toward the midfoot and forefoot during Parkinsonian walking, thereby enhancing the output signals in these regions. Figure 8(c) illustrates the complete signal transmission process, e.g., the raw signal is amplified and collected by a signal acquisition unit followed by Bluetooth transmission to a mobile device for visualization. In summary, the HPP LM/PAN-TENG-based pressure sensing system with signal acquisition capability provides a viable approach for the early detection of Parkinson's disease.

4 Conclusions

A stable encapsulation of LM within PAN fiber network was achieved by SBS of PAN simultaneously with LM spraying followed by hot-pressing, addressing the challenges in LM dispersion and oxidation leakage caused by its high surface tension. The hot-pressing process disrupted the native oxide layer on the LM surface, promoting the encapsulation of individual fibers and the formation of continuous thermal and electrical conduction pathways, thereby significantly enhancing overall performance. The resultant LM/PAN composite film achieved an in-plane thermal conductivity of 7.768 $W \cdot m^{-1} \cdot K^{-1}$, meeting the heat dissipation requirements for compact electronic devices. Furthermore, the highly conductive network constructed by LM endowed the film with an exceptional electromagnetic interference shielding effectiveness, reaching a total shielding effectiveness (SE_T) of 79.52 dB, suitable for lightweight and thin shielding applications. The film demonstrated rapid Joule heating, e.g., reaching 130.2 °C under a low applied voltage of 1.5 V while maintaining excellent temperature uniformity and operational stability. A TENG-based pressure sensor constructed from the LM/PAN film as the electrode and Ecoflex™ as the triboelectric layer delivered an output voltage of 211 V with outstanding durability to maintain 203 V after 1800 continuous cycles. The sensor effectively detected various human motions and accurately captured gait characteristics associated with Parkinson's disease, offering a novel strategy for early pathological diagnosis. The as-fabricated composite film offers a strategy for developing highly promising thermal management materials for applications in micro-electronics, flexible electromagnetic protection, and wearable health monitoring devices.

Electronic Supplementary Material: Supplementary material is available in the online version of this article at https://doi.org/10.26599/NR.2026.94908430.

Data availability

All data needed to support the conclusions in the paper are presented in the manuscript and the Electronic Supplementary Material. Additional data related to this paper may be requested from the corresponding author upon request.

Acknowledgement

This research was supported by the National Natural Science Foundation of China (No. 52503142), the Science and Technology Talents Service Enterprise Project of Hubei Province (No. 2025DJB017), the Key Research and Development Program of Hubei Province (No. 2025EIA062), the Science and Technology Planning Project of State Administration for Market Regulation (Nos. 2022MK084 and 2024MK182), and the Science and Technology Project of Hubei Province Market Supervision Administration (No. Hbscjg-KJ2022001).

Declaration of interest statement

All the contributing authors report no conflict of interests in this work.

Author contribution statement

Q. Z.: Data curation, investigation. J. Y. L.: Methodology, investigation. Z. Z.: Writing – original draft, funding acquisition. S. R. T.: Methodology, investigation. X. N. T.: Methodology, investigation. G. M. C.: Conceptualization, supervision. D. S. C.: Writing – review & editing, funding acquisition. X. W.: Conceptualization, supervision. All authors have given approval to the final version of the manuscript.

Use of AI statement

None.

References

[1] Deng, Y. G.; Jiang, Y.; Liu, J. Low-melting-point liquid metal convective heat transfer: A review. *Appl. Therm. Eng.* **2021**, *193*, 117021.

[2] Tan, S. R.; Wang, J. S.; Jin, W. H.; Zhang, Q.; Zhao, Z.; Li, D. Q.; Cheng, D. S.; Bi, S. G.; Ran, J. H.; Cai, G. M. et al. Multifunctional flexible conductive filament for human motion detection and electrothermal. *Compos. Commun.* **2023**, *37*, 101446.

[3] Zhuang, J.; Lv, J. L.; Jin, W. H.; Yu, Q.; Yu, J.; He, L.; Tang, X. N.; Ran, W. H.; Cai, G. M.; Cheng, D. S. et al. Multifunctional carboxymethyl cellulose nanofiber/liquid metal aerogels for sound absorption and heat insulation. *Cellulose* **2024**, *31*, 9253–9263.

[4] Ran, L. X.; Ma, X. G.; Qiu, L. J.; Sun, F. R.; Zhao, L. J.; Yi, L. F.; Ji, X. Y. Liquid metal assisted fabrication of MXene-based films: Toward superior electromagnetic interference shielding and thermal management. *J. Colloid Interface Sci.* **2023**, *652*, 705–717.

[5] Wang, J. S.; Wang, Y.; Jue, R.; Li, D. Q.; Zhao, Z.; Cai, G. M.; Cheng, D. S.; Wang, X. Liquid metal/CNT nanocomposite coated cotton fabrics for electromagnetic interference shielding and thermal management. *Cellulose* **2022**, *29*, 8907–8918.

[6] Zeng, Z. H.; Jiang, F. Z.; Yue, Y.; Han, D. X.; Lin, L. C.; Zhao, S. Y.; Zhao, Y. B.; Pan, Z. Y.; Li, C. J.; Nyström, G. et al. Flexible and ultrathin waterproof cellular membranes based on high-conjunction metal-wrapped polymer nanofibers for electromagnetic interference shielding. *Adv. Mater.* **2020**, *32*, 1908496.

[7] Zheng, Y.; Song, Y. J.; Gao, T.; Yan, S. Y.; Hu, H. H.; Cao, F.; Duan, Y. P.; Zhang, X. F. Lightweight and hydrophobic three-dimensional wood-derived anisotropic magnetic porous carbon for highly efficient electromagnetic interference shielding. *ACS Appl. Mater. Interfaces* **2020**, *12*, 40802–40814.

[8] He, Q. M.; Tao, J. R.; Yang, D.; Yang, Y.; Wang, M. Surface wrinkles enhancing electromagnetic interference shielding of copper coated polydimethylsiloxane: A simulation and experimental study. *Chem. Eng. J.* **2023**, *454*, 140162.

[9] Pavlou, C.; Pastore Carbone, M. G.; Manikas, A. C.; Trakakis, G.; Koral, C.; Papari, G.; Andreone, A.; Galiotis, C. Effective EMI shielding behaviour of thin graphene/PMMA nanolaminates in the THz range. *Nat. Commun.* **2021**, *12*, 4655.

[10] Wang, Y.; Gao, Y. N.; Yue, T. N.; Chen, X. D.; Che, R. C.; Wang, M. Liquid metal coated copper micro-particles to construct core-shell structure and multiple heterojunctions for high-efficiency microwave absorption. *J. Colloid Interface Sci.* **2022**, *607*, 210–218.

[11] Li, D. P.; Wang, P.; Li, Y. Y.; Yong, Z. Z.; Wu, K. J.; Zhang, Y.; Wang, J.; Hu, D. M. 3D-structured carbon nanotube fibers as ultra-robust fabrics for adaptive electromagnetic shielding. *Nano Res.* **2024**, *17*, 8521–8530.

[12] Abay, Z. M.; Wei, Y. X.; Tang, Z. G.; Liu, Y. G.; Chen, K.; Li, H.; Wang, Q. C.; Yuan, J.; Hu, P. P.; Lu, D. et al. Versatile MXene/(GO-AgNWs) electronic textile enabled by mixed-scale assembly strategy. *Nano Energy* **2025**, *139*, 110963.

[13] Zhou, G.; Yao, L.; Xie, Z. X.; Kamran, U.; Xie, J. W.; Zhang, F.; Park, S. J.; Zhang, Y. H. Controllable construction of CNT-Interconnected liquid metal networks for thermal management. *Compos. Part A: App. Sci. Manuf.* **2023**, *175*, 107743.

[14] Luo, W. M.; Wei, B. J.; Luo, T. L.; Li, B. W.; Zhu, G. M. 3D Network of liquid metal-embedded graphene via surface coating for flexible thermal management. *Small* **2024**, *20*, 2406574.

[15] Li, X. Y.; Lin, J.; Wu, J. W.; Liu, M. X.; Du, P. Y.; Xu, L.; Yan, D. X.; Jia, L. C.; Li, Z. M. Stretchable and leakage-free liquid metal networks for thermal management. *Adv. Funct. Mater.* **2025**, *35*, 2420839.

[16] Jiang, Z.; Yuan, Z. S.; Zhao, Y. M.; Xu, C. S.; Wang, Q. Flexible thermal interface materials with high dispersion of liquid metal in polyurethane induced by sodium alginate microcapsules. *Compos. Sci. Technol.* **2025**, *261*, 111041.

[17] Xu, H. C.; Liu, Y.; Mo, Y. P.; Chen, Z. Y.; Pan, X. J.; Bao, R. R.; Pan, C. F. All-fiber anti-jamming capacitive pressure sensors based on liquid metals. *Rare Met.* **2025**, *44*, 4839–4850.

[18] Yin, D. W.; Xiu, H. J.; Wang, S. M.; Pan, Y. F.; Li, N.; Cheng, R.; Huang, S. Y.; Fan, S.; Li, J. B. Flexible mille-feuille structure electromagnetic interference shielding film with excellent thermal conductivity and Joule heating. *Nano Res.* **2024**, *17*, 4544–4554.

[19] Duan, Y. S.; Yu, H. T.; Zhang, F.; Qin, M. M.; Feng, W. Preparation technologies for polymer composites with high-directional thermal conductivity: A review. *Nano Res.* **2024**, *17*, 9796–9814.

[20] Xie, K.; Zhang, Q.; Chen, F.; Fu, Q. Largely enhanced electromagnetic wave absorption via surface coating of carbonyl iron particles with liquid metal. *J. Mater. Chem. A* **2025**, *13*, 1887–1896.

[21] Cheng, Z. K.; Wang, H. Y.; Li, Z. W.; Yang, C.; Zhang, B. P.; Zhou, Y. Q.; Wang, Y. X.; Jia, C.; Li, L.; Wu, H. Processing nomex nanofibers by ionic solution blow-spinning for efficient high-temperature exhausts treatment. *Adv. Fiber Mater.* **2023**, *5*, 497–513.

[22] Jia, C.; Li, L.; Song, J. N.; Li, Z. W.; Wu, H. Mass production of ultrafine fibers by a versatile solution blow spinning method. *Acc. Mater. Res.* **2021**, *2*, 432–446.

[23] Xu, H. Y.; Tao, J.; Liu, Y.; Mo, Y. P.; Bao, R. R.; Pan, C. F. Fully fibrous large-area tailorable triboelectric nanogenerator based on solution blow spinning technology for energy harvesting and self-powered sensing. *Small* **2022**, *18*, 2202477.

[24] Pan, C. Q.; Lang, L.; Ran, J. H.; Tang, X. N.; Cheng, D. S.; Cai, G. M.; Wang, X. Design of micro/nano multilayer structure based on fabric for radiative cooling and infrared stealth. *Prog. Org. Coat.* **2025**, *208*, 109544.

[25] Zhang, X. B.; Wang, Y. F.; Tang, X. N.; Jin, W. H.; Mei, F.; Xu, Y.

Q.; He, L.; Wang, X.; Cheng, D. S. Metal-organic framework-based nanocomposite membrane for formaldehyde adsorption, antibacterial and food packaging. *Ind. Crops Prod.* **2025**, *236*, 121941.

[26] Zhang, B. P.; Li, Z. W.; Cheng, Z. K.; Li, L.; Yang, C.; Wang, H. Y.; Wu, H. Double-stretching as an effective and generalizable strategy towards thinner nanofibers in solution blow spinning. *Nano Res.* **2023**, *16*, 5709–5714.

[27] Tutak, W.; Sarkar, S.; Lin-Gibson, S.; Farooque, T. M.; Jyotsnendu, G.; Wang, D. B.; Kohn, J.; Bolikal, D.; Simon, C. G. The support of bone marrow stromal cell differentiation by airbrushed nanofiber scaffolds. *Biomaterials* **2013**, *34*, 2389–2398.

[28] Dadol, G. C.; Kilic, A.; Tijing, L. D.; Lim, K. J. A.; Cabatingan, L. K.; Tan, N. P. B.; Stojanovska, E.; Polat, Y. Solution blow spinning (SBS) and SBS-spun nanofibers: Materials, methods, and applications. *Mater. Today Commun.* **2020**, *25*, 101656.

[29] Gao, Y.; Zhang, J.; Su, Y.; Wang, H.; Wang, X. X.; Huang, L. P.; Yu, M.; Ramakrishna, S.; Long, Y. Z. Recent progress and challenges in solution blow spinning. *Mater. Horiz.* **2021**, *8*, 426–446.

[30] Song, J. N.; Li, Z. W.; Wu, H. Blowspinning: A new choice for nanofibers. *ACS Appl. Mater. Interfaces* **2020**, *12*, 33447–33464.

[31] Ma, Y. Q.; Zhou, R. Y.; Yang, M.; Zhang, J.; Song, W.; Ma, X.; Liu, M. Z.; Cui, X.; Li, B. K.; Zhang, Y. B. et al. Electrospinning-based bone tissue scaffold construction: Progress and trends. *Mater. Des.* **2025**, *252*, 113792.

[32] Kacem, E.; Suk, H. D.; Ponnamma, D.; Hassan, M. K.; Hawari, A.; Alshammari, B. A.; Al-Ejji, M. Exploring 3D printing and electrospinning technologies for advanced porous membrane fabrication: A review. *Adv. Mater. Technol.* **2025**, *10*, 70032.

[33] Ji, D. X.; Lin, Y. G.; Guo, X. Y.; Ramasubramanian, B.; Wang, R. W.; Radacsi, N.; Jose, R.; Qin, X. H.; Ramakrishna, S. Electrospinning of nanofibres. *Nat. Rev. Methods Primers* **2024**, *4*, 1.

[34] Keirouz, A.; Wang, Z.; Reddy, V. S.; Nagy, Z. K.; Vass, P.; Buzgo, M.; Ramakrishna, S.; Radacsi, N. The history of electrospinning: Past, present, and future developments. *Adv. Mater. Technol.* **2023**, *8*, 2201723.

[35] Li, Z. W.; Cui, Z. W.; Zhao, L. H.; Hussain, N.; Zhao, Y. Z.; Yang, C.; Jiang, X. Y.; Li, L.; Song, J. N.; Zhang, B. P. et al. High-throughput production of kilogram-scale nanofibers by Kármán vortex solution blow spinning. *Sci. Adv.* **2022**, *8*, eabn3690.

[36] Kramar, A.; Luxbacher, T.; González-Benito, J. Solution blow co-spinning of cellulose acetate with poly(ethylene oxide). Structure, morphology, and properties of nanofibers. *Carbohydr. Polym.* **2023**, *320*, 121225.

[37] Shen, C. Y.; Yang, Z. C.; Rao, J. S.; Wu, J.; Sun, C.; Sun, C. D.; Wu, D.; Chen, K. S. Chlorogenic acid-loaded sandwich-structured nanofibrous film developed by solution blow spinning: Characterization, release behavior and antimicrobial activity. *Food Packag. Shelf Life* **2022**, *32*, 100854.

[38] Gao, Y.; Xiang, H. F.; Wang, X. X.; Yan, K.; Liu, Q.; Li, X.; Liu, R. Q.; Yu, M.; Long, Y. Z. A portable solution blow spinning device for minimally invasive surgery hemostasis. *Chem. Eng. J.* **2020**, *387*, 124052.

[39] Yang, S. X.; Zhao, M.; He, R.; Chen, Y. X.; Guo, Y. Y.; Wang, H. Y.; Wang, Z. G.; Qiu, T.; Tuo, X. L. Solution blow spinning of the benzimidazole-containing aramid nanofibers for separators of lithium-ion batteries. *ACS Appl. Mater. Interfaces* **2024**, *16*, 15362–15371.

[40] Song, J. N.; Wang, H. Y.; Li, Z. W.; Long, Y. Z.; Liu, Z. L.; Wang, H. L.; Li, X. Y.; Fang, M. H.; Li, B.; Wu, H. Large-scale blow spinning of carbon microfiber sponge as efficient and recyclable oil sorbent. *Chem. Eng. J.* **2018**, *343*, 638–644.

[41] Wang, Q.; Yu, Y.; Yang, J.; Liu, J. Fast fabrication of flexible functional circuits based on liquid metal dual‐trans printing. *Adv. Mater.* **2015**, *27*, 7109–7116.

[42] Zhou, Z. Q.; Yu, Y.; Xu, G. L.; Liu, J.; Wang, Q. Hybrid transfer printing of liquid metals and allied inks for rapid fabrication of multifunctional soft electronics. *ACS Appl. Mater. Interfaces* **2024**, *16*, 25589–25599.

[43] Mao, Y. R.; Wu, Y. X.; Zhang, P. J.; Yu, Y.; He, Z. Z.; Wang, Q. Nanocellulose-based reusable liquid metal printed electronics fabricated by evaporation-induced transfer printing. *J. Mater. Sci. Technol.* **2021**, *61*, 132–137.

[44] Fang, R. Y.; Yao, B.; Chen, T. W.; Xu, X. W.; Xue, D. C.; Hong, W.; Wang, H.; Wang, Q.; Zhang, S. L. 3D highly stretchable liquid metal/elastomer composites with strain-enhanced conductivity. *Adv. Funct. Mater.* **2024**, *34*, 2310225.

[45] Bartlett, M. D.; Kazem, N.; Powell-Palm, M. J.; Huang, X.; Sun, W.; Malen, J. A.; Majidi, C. High thermal conductivity in soft elastomers with elongated liquid metal inclusions. *Proc. Natl. Acad. Sci. USA* **2017**, *114*, 2143–2148.

[46] Rahmani, P.; Shojaei, A.; Sakorikar, T.; Wang, M. X.; Mendoza-Apodaca, Y.; Dickey, M. D. Liquid metal nanoparticles physically hybridized with cellulose nanocrystals initiate and toughen hydrogels with piezoionic properties. *ACS Nano* **2024**, *18*, 8038–8050.

[47] Li, S.; Zhao, H. H.; Liu, M. H.; Zeng, X. F.; Wei, Y.; Zhang, G. G.; Liu, J.; Zhang, L. Q. Super-tough, super-elastic, temperature-responsive, and tunable viscoelastic elastomer enabled by embedding nanosized liquid metal droplets. *Compos. Sci. Technol.* **2023**, *244*, 110311.

[48] Lee, S.; Jaseem, S. A.; Atar, N.; Wang, M. X.; Kim, J. Y.; Zare, M.; Kim, S.; Bartlett, M. D.; Jeong, J. W.; Dickey, M. D. Connecting the dots: Sintering of liquid metal particles for soft and stretchable conductors. *Chem. Rev.* **2025**, *125*, 3551–3585.

[49] Majidi, C.; Alizadeh, K.; Ohm, Y.; Silva, A.; Tavakoli, M. Liquid metal polymer composites: From printed stretchable circuits to soft actuators. *Flex. Print. Electron.* **2022**, *7*, 013002.

[50] Guymon, G. G.; Malakooti, M. H. Multifunctional liquid metal polymer composites. *J. Polym Sci.* **2022**, *60*, 1300–1327.

[51] Yang, J. Y.; Yan, Y.; Huang, L. Z.; Ma, M. G.; Li, M. F.; Peng, F.; Huan, W. W.; Bian, J. Conductive eutectogels fabricated by dialdehyde xylan/liquid metal-initiated rapid polymerization for multi-response sensors and self-powered applications. *ACS Nano* **2025**, *19*, 2171–2184.

[52] Liu, Z.; Liu, L. L.; Guan, L.; Zhu, Y. J.; Lin, M. M.; Li, Q. L.; Guo, X. Q.; Wang, Z. Y.; Lian, Y. H.; Chen, P. et al. Elastic liquid metal composite with strain-independent EMI shielding properties. *J. Mater. Sci. Technol.* **2025**, *235*, 146–155.

[53] Liu, M. X.; Zhang, H. R.; Zhang, Z. Y.; Zhang, K. L.; Chen, Z. W.; Pan, L.; Zhou, J. T. Jujube-cake inspired lightweight and flexible MXene/liquid metal/bacterial cellulose electromagnetic interference shielding film with excellent Joule heating and thermal conductivity. *Compos. Sci. Technol.* **2024**, *255*, 110722.

[54] Liu, H. B.; Fu, R. L.; Su, X. Q.; Wu, B. Y.; Wang, H.; Xu, Y.; Liu, X. H. Electrical insulating MXene/PDMS/BN composite with enhanced thermal conductivity for electromagnetic shielding application. *Compos. Commun.* **2021**, *23*, 100593.

[55] Chen, L. J.; Ning, F. G.; Jin, L.; Wu, J.; Jiang, G. M.; Ma, P. B.; Yu, H.; Wang, F. M.; Wang, Z. L.; Chen, C. Y. Bionic double-helix braided ultra-stretchable energy-harvesting yarns for power and wearable electronics. *Nano Energy* **2025**, *138*, 110832.

[56] Dong, Z. J.; Hou, R. H.; Jiang, H.; Wang, W. J.; Zhang, F.; Zhao, G.; Chen, C. Y.; Ma, P. B. Hybrid thermoelectric-triboelectric smart knitted fabric for real-time monitoring of vascular crisis and postoperative recovery of severed fingers. *Mater. Des.* **2025**, *251*, 113669.